

## Observation of orbital angular momentum in the chiral magnet CrNb<sub>3</sub>S<sub>6</sub> by soft x-ray magnetic circular dichroism

M. Mito,<sup>1,2,\*</sup> H. Ohsumi,<sup>3</sup> T. Shishidou,<sup>4,†</sup> F. Kuroda,<sup>5</sup> M. Weinert,<sup>4</sup> K. Tsuruta,<sup>6</sup> Y. Kotani,<sup>6</sup> T. Nakamura,<sup>6</sup> Y. Togawa,<sup>2,7</sup> J. Kishine,<sup>2,8</sup> Y. Kousaka,<sup>2,7</sup> J. Akimitsu,<sup>9</sup> and K. Inoue<sup>2,10,11</sup>

<sup>1</sup>Graduate School of Engineering, Kyushu Institute of Technology, Kitakyushu 804-8550, Japan

<sup>2</sup>Center for Chiral Science, Hiroshima University, Higashihiroshima 739-8526, Japan

<sup>3</sup>RIKEN SPring-8 Center, Hyogo 679-5148, Japan

<sup>4</sup>Department of Physics, University of Wisconsin-Milwaukee, Milwaukee, Wisconsin 53201, USA

<sup>5</sup>Institute of Scientific and Industrial Research, Osaka University, Osaka 567-0047, Japan

<sup>6</sup>Japan Synchrotron Radiation Research Institute (JASRI), Hyogo 679-5198, Japan

<sup>7</sup>Graduate School of Engineering, Osaka Prefecture University, Sakai 599-8531, Japan

<sup>8</sup>Graduate School of Arts and Sciences, The Open University of Japan, Chiba 261-8586, Japan

<sup>9</sup>Research Institute for Interdisciplinary Science, Okayama University, Okayama 700-8530, Japan

<sup>10</sup>Graduate School of Science, Hiroshima University, Higashihiroshima 739-8526, Japan

<sup>11</sup>Institute for Advanced Materials Research, Hiroshima University, Higashihiroshima 739-8526, Japan



(Received 9 April 2019; published 29 May 2019)

The chiral magnet CrNb<sub>3</sub>S<sub>6</sub> with its solitonic objects has novel magnetic and transport properties, in which the spin-orbit coupling (SOC) plays a central role. Aiming to address the possible existence of orbital moments driven by SOC, we perform soft x-ray magnetic circular dichroism spectroscopy at the Cr  $L_{2,3}$  edges with in-plane magnetization. The dichroic signals provide direct experimental evidence that the Cr orbital magnetic moment is not quenched and is coupled antiparallel to the spin counterpart. Application of the orbital sum rule reveals that the magnitude of the Cr orbital moment is about 1% of the total magnetization. These findings are consistent with the first-principles electronic structure calculations that utilize the Cr  $2p$  core radial function to define the Cr local  $3d$  quantities. The distinct roles of the atomic SOC among the Cr  $3d$  and Nb  $4d$  states are discussed.

DOI: [10.1103/PhysRevB.99.174439](https://doi.org/10.1103/PhysRevB.99.174439)

### I. INTRODUCTION

The monoaxial chiral helimagnet CrNb<sub>3</sub>S<sub>6</sub> has attracted intensive interest with regard to its solitonic spin texture. The Dzyaloshinskii-Moriya (DM) interaction [1,2], driven by the spin-orbit coupling (SOC) and crystalline chirality, leads to intriguing phenomena. The magnetic ground state is a long-wavelength spiral order of Cr spins: magnetic moments, aligned ferromagnetically in the hexagonal  $ab$  plane, form a magnetic helix along the  $c$  axis with the handedness imprinted by the crystal chirality. Applying a relatively small magnetic field  $H$  perpendicular to the  $c$  axis drastically changes the magnetic configuration from a homogeneous spiral to the soliton kink structure—termed the chiral soliton lattice (CSL) [3–5]—and eventually to the forced ferromagnetic (FM) state at a critical magnetic field  $H_c$  of a few kOe [6]. Negative magnetoresistance has been observed in the CSL phase [7,8].

In CrNb<sub>3</sub>S<sub>6</sub>, Cr atoms intercalate in the layered parent 2H<sub>a</sub>-NbS<sub>2</sub> compound forming a planar  $\sqrt{3} \times \sqrt{3}$  superstructure [see Fig. 1(a)]. The stacking sequence along the  $c$  axis—whether the Cr atoms occupy  $2d$  or  $2c$  Wyckoff sites in the Sohncke [9,10] space group  $P6_322$ —determines the

crystalline chirality. Nb atoms split into two groups, those preserving their ideal positions ( $2a$  site) and those with their  $z$  coordinates slightly deviating from 0 or 1/2 ( $4f$  site), as shown in Table I. Each Cr has six nearest-neighbor sulfurs and two Nb ( $4f$ ) atoms at distances of 2.35 and 3.06 Å, respectively [see Figs. 1(a) and 1(b)] [11]. In this cluster unit CrS<sub>6</sub>-Nb<sub>2</sub> the local symmetry around Cr is approximately  $D_{3d}$  and the Cr  $3d$  orbitals show an energy splitting  $t_{2g} \rightarrow e'_g + a_{1g}$  as in Fig. 1(c). (Although the actual site symmetry is  $D_3$ , we will use this notation to be consistent with previous work.) Here  $a_{1g}$  is a  $3z^2 - r^2$  orbital aligned along the  $c$  axis toward Nb ( $4f$ ) atoms. A localized picture with electron configuration  $(t_{2g})^3$  [or  $(e'_g)^2(a_{1g})^1$ ] with a nominal valency Cr<sup>3+</sup> is often considered since it provides a local moment  $S = 3/2$  consistent with the observed magnetic moment  $\sim 3\mu_B$  ( $2.9\mu_B$  [6],  $3.2\mu_B$  [12]).

Provided that the SOC is weak compared to other interactions (e.g., crystalline field, orbital hybridization, and exchange interaction), the DM interaction arises from a combined second-order perturbation of the SOC and (twisted) exchange interaction, and thus the DM is linear in SOC. On the other hand, magnetocrystalline anisotropy (MCA) and unquenched orbital magnetic moments arise from SOC alone. In CrNb<sub>3</sub>S<sub>6</sub>, although the MCA has been known to be easy-plane type [6], the orbital magnetic moment has never been measured experimentally. Indeed, the magnetic ordering

\*mitoh@mns.kyutech.ac.jp

†shishido@uwm.edu

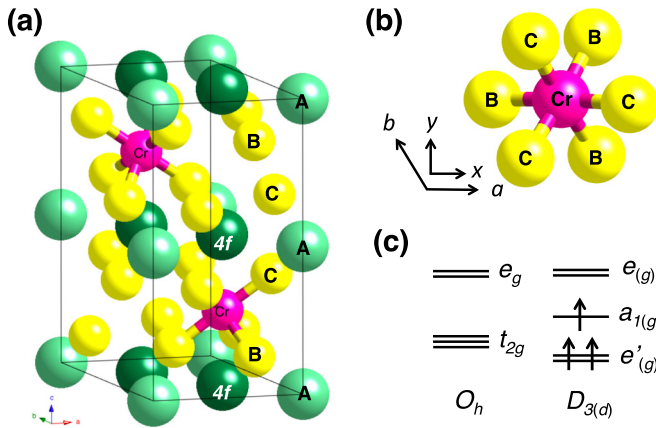


FIG. 1. (a) Crystal structure of  $\text{CrNb}_3\text{S}_6$ . The host  $\text{NbS}_2$  forms a two-dimensional triangular layer with S-Nb-S stacking sequence of (B-A-B) (C-A-C) (B-A-B) . . . There are two Cr atoms per unit cell (shown by red spheres), which occupy the  $2d$  site. Nb atoms at a  $4f$  site are drawn in dark green. (b) Top view of  $\text{CrS}_6$  cluster with definition of planar axes. (c) Crystalline field splitting of Cr  $3d$  level.

temperature  $T_c$  of  $\text{CrNb}_3\text{S}_6$  was evaluated to be approximately 130 K [6,11,13]. Recently, the interplane exchange interaction along the chiral  $c$  axis ( $J_{\parallel}/k_B = 16.2$  K), the DM interaction ( $D/k_B = 1.29$  K), and the easy-plane anisotropy ( $K_{\text{perp}}/k_B = 1.02$  K) have been evaluated from the ESR experiment [14], showing fair agreement with the estimated values from the magnetization curve [15]. It is expected that analyzing these quantities will reveal how the SOC manifests itself in  $\text{CrNb}_3\text{S}_6$  and further would provide a clue to understand the microscopic origin of the DM interaction.

Here we report x-ray magnetic circular dichroism (XMCD) measurements at the Cr  $L_{2,3}$  edges ( $2p \rightarrow 3d$  photoabsorption) in the forced FM state with the external field perpendicular to the  $c$  axis. Utilizing the Cr  $2p$  core state, which is highly localized around the nucleus, as a local probe, the XMCD measurement provides direct information about the Cr local spin and orbital magnetic moments induced in the Cr  $3d$  shell. It is found that the  $3d$  orbital moment is small but finite and is coupled antiparallel to the spin counterpart, consistent with the density functional theory (DFT) calculations that we report here.

Both in the experimental and theoretical studies we carry out, quantitative determination of the Cr  $3d$  spin and orbital moments is, however, not straightforward. The so-called XMCD spin sum rule [16] is not directly applicable to the present case: Cr is a light transition-metal atom and its  $2p$

core spin-orbit splitting ( $\sim 8$  eV) is not large enough to prevent quantum-mechanical mixing between the  $2p_{3/2}$  and  $2p_{1/2}$  excitations ( $j$ - $j$  mixing) caused by the  $2p$ - $3d$  Coulomb interaction in the photoabsorption final states [17]. Thus the fundamental assumption behind the spin sum rule—that the  $L_3$  and  $L_2$  edges are well separated in energy and identified as pure  $2p_{3/2}$  and  $2p_{1/2}$  excitations respectively—is violated to a considerable extent. We examine a correction method [18] proposed by Goering for the spin sum rule that uses the branching ratio of the  $L_2$  to  $L_3$  edges in the x-ray absorption spectrum (XAS) for unpolarized light (i.e.,  $2/4$  in the no mixing case), but find it is unsuccessful in the present case. Furthermore, the effective magnetic moment per Cr calculated from the Curie constant is approximately  $4\mu_B$  ( $3.92\mu_B$  [6],  $4.4\mu_B$  [12],  $4.1$ – $4.3\mu_B$  [19]). As for the number of holes in the  $3d$  shell ( $n_h$ ), the nominal value of  $n_h = 7$  is unreasonable, and we therefore use DFT calculations to derive optimal  $n_h$  values.

On the other hand, the orbital sum rule [20], which does not rely on a distinction between the  $L_3$  and  $L_2$  edges, should be applicable to the present case. Our main focus in the XMCD measurement is, therefore, the evaluation of the Cr  $3d$  orbital moment. Nevertheless, care is needed in applying either of these sum rules since both are vulnerable to errors in the normalization and background correction to the absorption intensity.

In the DFT calculations, the information regarding the spin and orbital moments is provided as a density distribution calculated from a corresponding operator  $\mathbf{A}$  and band spinors  $\psi_i(\mathbf{r})$ ,  $\mathbf{A}(\mathbf{r}) = \sum_i \psi_i^\dagger \mathbf{A} \psi_i$  which is a continuous function of  $\mathbf{r}$ . The idea of atomlike Cr local moments is ill-defined since their values depend on the region used to integrate  $\mathbf{A}(\mathbf{r})$ . Furthermore, there is strong hybridization of Cr  $3d$  states with S  $3p$  and Nb  $4d$  states that makes the separation of a Cr  $3d$  shell ill-defined. To cope with these difficulties, we resort to the fact that the Cr  $L_{2,3}$  XAS/XMCD measurements employ the Cr  $2p$  core state as a local probe to detect the Cr  $3d$  states, and develop a method to define and calculate the Cr  $3d$  components in the DFT orbitals  $\psi_i(\mathbf{r})$  through a projection on to the Cr  $2p$  core wave functions, mimicking the experimental situation.

The rest of this paper is organized as follows. In Sec. II, the XAS/XMCD sum rules are reviewed, and from there, the definition of Cr local  $3d$  quantities used in the DFT calculations is provided. Section III is devoted to describing experimental procedures. In Sec. IV, XMCD results at the Cr  $L_{2,3}$  edges are provided, and in Sec. V, the DFT results are shown. Section VI provides concluding remarks.

## II. $3d$ MOMENTS PROBED BY $2p$ CORE STATES

Consider the electric-dipole ( $E1$ ) transition from the Cr  $2p$  core to the Cr  $3d$  valence shell. Assume that these states are expressed by *single* normalized radial functions,  $R_i$  ( $i = 2p, 3d$ ),  $\langle R_i | R_i \rangle = 1$ , ignoring their energy dependency. Starting from the Fermi “golden rule” for the  $E1$  transition and applying the Wigner-Eckart theorem, it can be shown [16,20] that the integrated photoexcitation spectra are related to the orbital

TABLE I. Structural parameters of  $\text{CrNb}_3\text{S}_6$  taken from Ref. [11].

Space group no. 182, $P6_322$ , $a = 5.7134 \text{ \AA}$ , $c = 12.0563 \text{ \AA}$		
Element	Wyckoff	internal position
Cr	$2d$	( $2/3, 1/3, 1/4$ )
Nb	$2a$	( $0,0,1/2$ )
Nb	$4f$	( $1/3, 2/3, 0.4962$ )
S	$12i$	( $0.318\ 36, -0.012\ 52, 0.632\ 63$ )

and spin magnetic moments of the Cr  $3d$  shell ( $m_{\text{orb}}$  and  $m_{\text{spin}}$  in unit of  $\mu_B$ ):

$$\int (\mu_+ - \mu_-) d\omega = \frac{1}{2} \kappa m_{\text{orb}}, \quad (1)$$

$$\int_{j_+} (\mu_+ - \mu_-) d\omega - 2 \int_{j_-} (\mu_+ - \mu_-) d\omega = \frac{1}{3} \kappa m_{\text{spin}}, \quad (2)$$

$$\int (\mu_+ + \mu_- + \mu_0) d\omega = \kappa n_h, \quad (3)$$

where  $\mu_+$  and  $\mu_-$  denote absorption coefficients of circularly polarized x rays that propagate along the magnetization direction with positive and negative helicities ( $\sigma_+$  and  $\sigma_-$ ), respectively,  $\mu_0$  for x rays linearly polarized along the magnetization direction, and  $\kappa$  is a normalization constant. The  $E1$  transition operator involved in each  $\mu_q$  ( $q = +1, -1, 0$ ) is expressed as  $\sqrt{4\pi/3} rY_{1q}(\mathbf{r})$ , with the  $z$  axis taken along the magnetization direction. Equations (1) and (2) are sum rules regarding the XMCD spectra, while (3) is for XAS with unpolarized light. In the spin sum rule, Eq. (2), we omit for simplicity the contribution from the spin magnetic dipole [16]. It is important to note that a further assumption—final states are classified into pure  $j_+(2p_{3/2})$  and  $j_-(2p_{1/2})$  excitations and the  $L_3$  and  $L_2$  edges are well separated in energy—is involved in Eq. (2); the XMCD spectrum has to be integrated separately at each edge. The common proportionality constant  $\kappa$ , which is experimentally unknown, is given by a dipole radial matrix element squared,

$$\kappa = \langle R_{2p} | r | R_{3d} \rangle^2. \quad (4)$$

By dividing (1) and (2) by (3), the constant  $\kappa$  is eliminated from the expressions:

$$\frac{\int (\mu_+ - \mu_-) d\omega}{\int (\mu_+ + \mu_- + \mu_0) d\omega} = \frac{1}{2} \frac{m_{\text{orb}}}{n_h}, \quad (5)$$

$$\frac{\int_{j_+} (\mu_+ - \mu_-) d\omega - 2 \int_{j_-} (\mu_+ - \mu_-) d\omega}{\int (\mu_+ + \mu_- + \mu_0) d\omega} = \frac{1}{3} \frac{m_{\text{spin}}}{n_h}, \quad (6)$$

which can be used to evaluate the individual  $m_{\text{orb}}$  and  $m_{\text{spin}}$  (per hole). On the other hand, the ratio of  $m_{\text{orb}}$  to  $m_{\text{spin}}$  is found from the XMCD spectrum alone. Equation (1) divided by (2) yields

$$\frac{\int (\mu_+ - \mu_-) d\omega}{\int_{j_+} (\mu_+ - \mu_-) d\omega - 2 \int_{j_-} (\mu_+ - \mu_-) d\omega} = \frac{3}{2} \frac{m_{\text{orb}}}{m_{\text{spin}}} \quad (7)$$

and contains neither  $\kappa$  nor  $n_h$ .

The derivations of the sum rules explicitly assume that the Cr  $3d$  orbitals will contribute a total of ten electrons to the (occupied and unoccupied) bands, and that  $\kappa$  provides the normalization needed to relate experiments and theory. Equation (4) dictates that the XAS/XMCD measurement employs a localized atomic function  $rR_{2p}$  in probing the Cr  $3d$  states. The difficulty is in defining the normalized  $3d$  functions  $R_{3d}$ . To avoid this issue, we propose to calculate the matrix elements coupling the  $2p$  core levels and the valence states  $\psi_i$ , similar to those that actually occur in the Fermi golden rule

$$\langle rR_{2p} Y_{2,m} \chi_\sigma | \psi_i \rangle \equiv \langle rR_{2p}; m, \sigma | \psi_i \rangle, \quad (8)$$

where the projection onto the spherical harmonics  $Y_{\ell m}$  and spinor  $\chi_\sigma$  takes into account the dipole selection rules, i.e., including the product of the core function and the  $E1$  operator. In the case that  $\psi_i$  depends only on atomiclike Cr  $3d$  orbitals, then (the square of) these matrix elements are simply  $\kappa$  as defined in Eq. (4). These matrix elements, which are effectively projections of the Cr  $3d$  states onto the  $2p$  cores, are well defined since the region of integration is naturally limited by the spatial extent of the localized  $2p$  core state, and are determined by the ( $\ell = 2$ ) partial wave expansion of the valence wave functions, which are also well defined. (The radial function  $R_{2p}$  corresponds to the  $p_{1/2}$  or  $p_{3/2}$  states as appropriate.)

To proceed, we first define a density matrix constructed from bands  $\psi_i$  below an energy  $E$ ,

$$\rho(E) = \sum_i \theta(E - E_i) |\psi_i\rangle \langle \psi_i|, \quad (9)$$

and a weighted density matrix

$$\tilde{n}_{m\sigma, m'\sigma'}(E) = \langle rR_{2p}; m, \sigma | \rho(E) | rR_{2p}; m', \sigma' \rangle, \quad (10)$$

which includes the matrix elements, Eq. (8). The trace of this density matrix gives the effective number,  $\tilde{n}(E)$ , of  $3d$  electrons below an energy  $E$ , and is simply related to the nominal number of  $3d$  electrons,  $n^{(3d)}(E)$ , by

$$\tilde{n}(E) = \tilde{\kappa} n^{(3d)}(E). \quad (11)$$

Again, if the simplified assumptions regarding  $R_{3d}$  are satisfied, then  $\kappa$  and  $\tilde{\kappa}$  would be equivalent.

The final step is to provide a normalization of  $\tilde{\kappa}$ . There exists an energy  $E_c$  ( $> E_F$ ) that separates the  $3d$  and  $4d$  manifolds; this energy can be determined by inspecting the local density of states and the nodal structure of the radial wave functions (i.e., the  $4d$  radial functions have an additional radial node). By imposing the condition that the  $3d$  states contribute ten electrons,  $n^{(3d)}(E_c) = 10$ , we arrive at the following formula for the  $3d$  density matrix expressed solely in terms of  $\tilde{n}$  and thus is readily calculated from the DFT orbitals:

$$n^{(3d)}(E_F) = \frac{10}{\tilde{n}(E_c)} \tilde{n}(E_F). \quad (12)$$

The present DFT method to calculate  $3d$  moments from Eq. (12) is more in line with the XAS/XMCD experiment than other computational schemes (e.g., the use of certain integration range for  $\mathbf{A}(\mathbf{r})$  or use of maximally localized Wannier functions [21]); both the experiment and the present theory rely on the localized radial function  $rR_{2p}$  to extract the  $3d$  contributions. Therefore, the ground state  $m_{\text{spin}}$  and  $m_{\text{orb}}$  calculated using the present theory should represent the experiments well as long as the sum-rule application on the experimental side is not deteriorated due to background removal errors and/or final-state  $j$ - $j$  mixing.

### III. EXPERIMENTAL PROCEDURES

Micron-size crystals typically  $10 \times 10 \times 1 \mu\text{m}^3$  were cut from a bulk single crystal CrNb<sub>3</sub>S<sub>6</sub> by using an focused ion beam technique, and the thickness of the center was reduced down to approximately 100 nm [22]. These were mounted on a Ta substrate with a 5- $\mu\text{m}$ -diameter pinhole using W, as

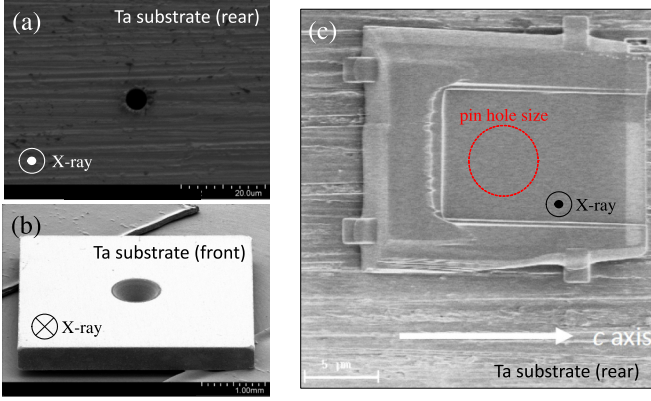


FIG. 2. (a),(b) Ta substrate (rear and front panel) and (c) microprocessed  $\text{CrNb}_3\text{S}_6$  thin specimen mounted in the rear panel of Ta substrate. In (c), the pin hole size with the  $5\text{-}\mu\text{m}$  diameter is displayed.

shown in Fig. 2. Since the Ta does not allow the x rays to pass, we obtain magnetic information only for the thin part of the sample. The XAS/XMCD spectroscopy was carried out using beam line BL25SU of SPring-8 [23]. The photoabsorption spectra were obtained by directly measuring the intensity of the transmitted light. The Ta substrate with microprocessed specimen was placed on the sample holder specified to the XMCD platform in contact with indium foil to maintain sufficient thermal conductivity. The measurements were performed at 10 K, which is sufficiently lower than  $T_c \sim 130$  K. The magnetic field  $H$  of  $\pm 4$  kOe, which by far exceeds  $H_c \sim 2$  kOe, was applied perpendicularly to the chiral axis ( $c$  axis) to realize a forced FM state with in-plane magnetization. The x-ray beam was almost parallel to  $H$ . In order to minimize possible artifacts caused by the asymmetry of experimental setups, we took an average of the spectra measured at  $H = \pm 4$  kOe;  $\mu(+)=\{\mu(\sigma_+, +H)+\mu(\sigma_-, -H)\}/2$  and  $\mu(-)=\{\mu(\sigma_-, +H)+\mu(\sigma_+, -H)\}/2$  were employed in the present study. Note that  $\mu(+)$  and  $\mu(-)$  are the spectra with photon spin parallel and antiparallel to the magnetic field, respectively. In applying the sum rules, we define the following four integrals:

$$\int [\mu(+)-\mu(-)]d\omega = A, \quad (13)$$

$$\int [\mu(+)+\mu(-)]d\omega = B, \quad (14)$$

$$\int_{j_+} [\mu(+)-\mu(-)]d\omega = C, \quad (15)$$

$$\int_{j_-} [\mu(+)-\mu(-)]d\omega = D, \quad (16)$$

where  $A = C + D$ . Approximating the integral of unpolarized XAS,  $\int(\mu_+ + \mu_- + \mu_0)d\omega \simeq \frac{3}{2} \int(\mu_+ + \mu_-)d\omega = \frac{3}{2}B$ , we rewrite Eqs. (5)–(7) as

$$A/\left(\frac{3}{2}B\right) = \frac{1}{2} \frac{m_{\text{orb}}}{n_h}, \quad (17)$$

$$(C - 2D)/\left(\frac{3}{2}B\right) = \frac{1}{3} \frac{m_{\text{spin}}}{n_h}, \quad (18)$$

TABLE II. Sum-rule based estimations of  $A$ ,  $B$ ,  $C$ , and  $D$ .

$A$	$B$	$C$	$D$
$-0.031\ 102$	$10.514$	$0.241\ 67$	$-0.272\ 77$

$$A/(C - 2D) = \frac{3}{2} \frac{m_{\text{orb}}}{m_{\text{spin}}}. \quad (19)$$

In the next section, the values of  $A$  to  $D$  are estimated and given in Table II.

The DFT calculations were performed assuming ferromagnetic spin configuration with the crystal structure [11] determined experimentally at ambient pressure (summarized in Table I). The all-electron full-potential linearized augmented plane-wave (FLAPW) method [24] as implemented in the HiLAPW code was used. The muffin-tin sphere radius was set to  $1.1 \text{ \AA}$  for all atoms. The plane-wave cutoffs were 16 and 200 Ry for the wave function and potential, respectively. The Perdew, Burke, and Ernzerhof form of the generalized gradient approximation (GGA) [25] was used for exchange correlation. The Brillouin zone was sampled with a  $20 \times 20 \times 20$   $k$ -point mesh. The SOC was handled in two different ways: included in each self-consistent cycle or only in the last cycle. Both results were practically identical with regard to the magnetic moments and the MCA energy. The radial function  $R_{2p}$  needed to calculate the Cr  $3d$  quantities was obtained from a scalar-relativistic calculation of Cr  $2p$  core state (i.e., no difference between  $2p_{3/2}$  and  $2p_{1/2}$ ) under a spherical and spin-averaged part of the self-consistent potential.

#### IV. XMCD RESULTS

Figure 3 shows the XAS spectra  $\mu(+)$  and  $\mu(-)$  measured at 10 K, which are characterized by two-peak structure embedded in a broad almost linear background with a negative

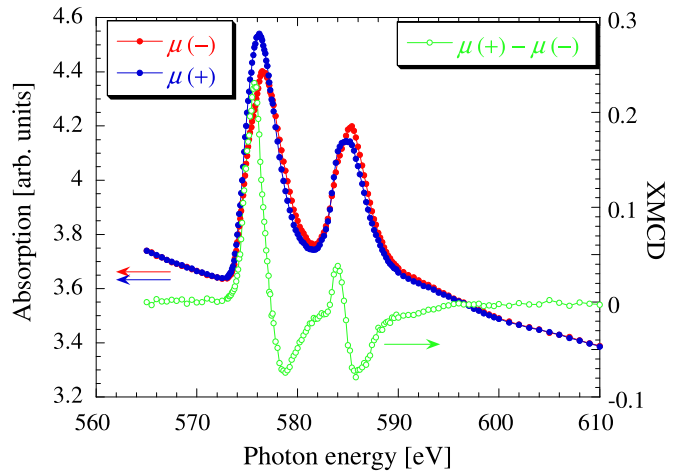


FIG. 3. Polarized XAS spectra of  $\text{CrNb}_3\text{S}_6$  at 10 K for  $H = \pm 4$  kOe.  $\mu(+)$  and  $\mu(-)$  represent the XAS with the photon spin parallel and antiparallel to the external magnetic field, respectively. The MCD spectrum is defined as  $\mu(+)-\mu(-)$ . The Cr  $L_3$  and  $L_2$  edges produce XAS peaks around 577 and 585 eV, respectively.

slope. The peaks located around 577 and 585 eV are assigned to the Cr  $L_3$  and  $L_2$  edges, respectively. For photon energies from 572 to 596 eV, the XMCD spectrum defined as  $\mu(+)-\mu(-)$  shows characteristic signals. The spectrum exhibits a dispersive line shape at each of the  $L_3$  and  $L_2$  edges: it starts with a sharp positive peak followed by a negative hump. In the  $L_3$  region, the positive signals prevail over the negative ones. By contrast, for the  $L_2$  edge, the negative signals in the hump dominate over the positive signals of the precursor peak. The alternating sign of the dominant XMCD signals from positive (at the  $L_3$  edge) to negative ( $L_2$ ) is consistent (based on the transition probability from the  $2p$  core state to the empty states in the  $3d$  shell) with the fact that the positive  $m_{\text{spin}}$  (negative spin angular momentum) is induced in the  $3d$  shell in the ground state. (See Ref. [26] and Appendix A.) Note that the positive peak in the  $L_2$  region is much weakened compared to that in the  $L_3$  edge and overlaps with the  $L_3$  negative hump.

Figure 4(a) shows the photon energy dependence of  $\mu(+)+\mu(-)$ . It has a background, which is constructed with the combination of two linearlike terms and two arctangent functions. As explained below, reasonable consideration of background contributions enables us to estimate  $B$ , so that we can estimate the denominator in the sum rules Eqs. (17) and (18), i.e.,  $\frac{3}{2}B$ . At first, we assume an almost linear background contribution [black line in Fig. 4(a)], termed bkg. (1), so that the residual spectra for  $< 568$  eV and  $> 592$  eV have constant values as shown with the green data in Figs. 4(a) and 4(b). Next, we consider a background component, termed bkg. (2), consisting of two arctangent functions centered at the edge jumps, as shown with purple data in Fig. 4(b). The ratio of arctangent background for  $L_3$  and that for  $L_2$  is assumed to be 5:3, so that it becomes consistent with the intensity ratio of intrinsic  $L_3$  and  $L_2$  photoabsorption (1.6 : 1.0). Removing all the background, the residual spectra termed  $Y$  is shown in Fig. 4(b) by the dark-green color. Its integral with respect to the energy, shown with light red in Fig. 4(b), yields  $B \sim 10.514$ .

For the next step, we consider the calculation of the numerator of Eq. (17). Figure 5 shows the XMCD spectrum and its integral with respect to the photon energy. In the case of estimating a small integration value, the scatter in the data may result in an indispensable estimation error. Thus, after smoothing the XMCD data for  $< 572$  eV and  $> 596$  eV, we integrated them against the energy to estimate  $A$  in Eq. (13). We evaluated  $A$  to be  $-0.031102$  (Table II), and obtained  $m_{\text{orb}}/n_h = 2A/(\frac{3}{2}B) = -3.944 \times 10^{-3}$ . The errors in estimating  $A$  and  $B$  are estimated to be  $\pm 10\%$  (by varying the smoothing range) and  $\pm 7\%$  (by varying the background contribution), respectively, so that  $m_{\text{orb}}/n_h$  has the error of  $\pm 12\%$ .

Third, we attempt to estimate two integral values of the XMCD,  $C$  and  $D$  appearing in Eq. (18). As we have seen in Fig. 3, the XMCD spectrum consists of two dispersive structures, one in the lower energy side ( $L_3$ ) and the other higher energy side ( $L_2$ ). Although the two structures are overlapping, we propose a tentative border between the  $L_3$  area and the  $L_2$  one at 581.3 eV in Fig. 4(b), and do the integration of XMCD for both lower and higher energy sides. Consequently we obtain  $C = 0.24167$  [Eq. (15)] and  $D = -0.27277$  [Eq. (16)], resulting in  $m_{\text{spin}}/n_h = 1.498 \times 10^{-1}$  according to Eq. (18). If we adopt  $n_h = 7$ , based on the

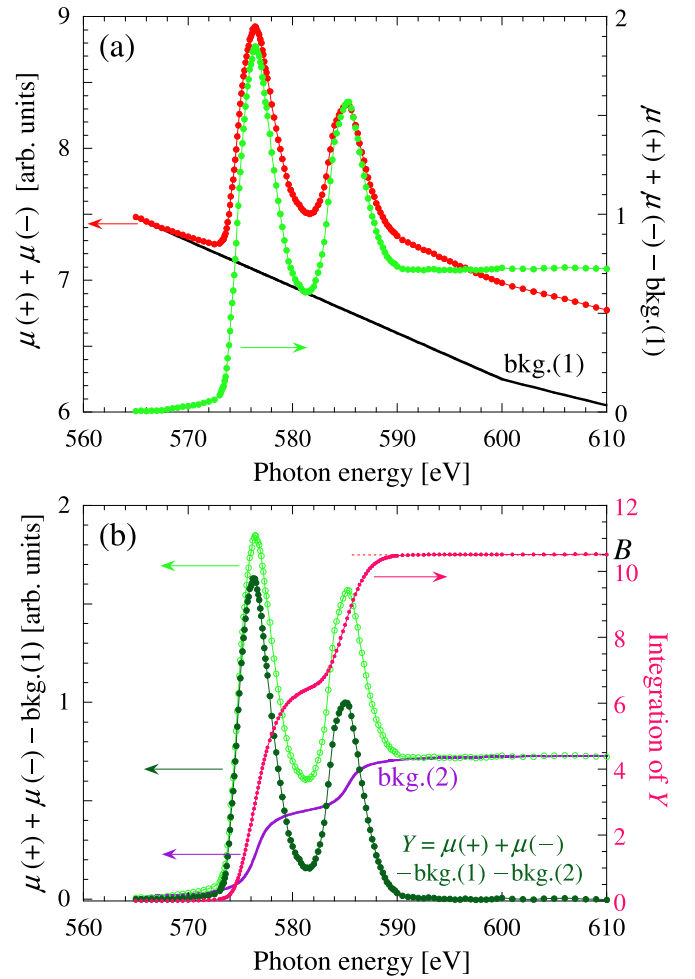


FIG. 4. (a) The spectra of  $\mu(+)+\mu(-)$ . Also shown, the spectra of  $\mu(+)+\mu(-)$  after subtracting linearlike background bkg. (1). (b) Consideration of arctangent background components, bkg. (2), for the spectrum of  $\mu(+)+\mu(-)$  and the integration of the residual spectrum  $Y [= \mu(+)+\mu(-) - \text{bkg. (1)} - \text{bkg. (2)}]$  with respect to the energy. The ratio of arctangent background for  $L_3$  and  $L_2$  became approximately 5 : 3, consistent with the ratio (1.6 : 1.0) of the  $Y$  intensity for  $L_3$  and that for  $L_2$ . The full width at half maximum for  $Y$  of  $L_3$  is almost the same as that for  $Y$  of  $L_2$ ; there is a minimum of their overlap at 581.3 eV. The integration value of  $Y$  corresponds to  $B$  in Eq. (14).

nominal valency of  $\text{Cr}^{3+}$  and the magnetization measurements [6] and considered to be an upper bound of  $n_h$ , we obtain  $m_{\text{orb}} = -2.761 \times 10^{-2} \mu_B$ , and  $m_{\text{spin}} = 1.048 \mu_B$ , as shown in Table III. Note that the estimated  $m_{\text{spin}}$  is far smaller than the expected value of  $3 \mu_B$ . Even if the  $L_3$ - $L_2$  boundary is shifted toward the lower energy side, for instance 580.3 eV, there is only a small increase in  $m_{\text{spin}}/n_h$  to  $1.676 \times 10^{-1}$  ( $C = 0.27292$  and  $D = -0.30402$ ), and  $m_{\text{spin}}$  for  $n_h = 7$  increases just to 1.173. According to Goering's sum-rule correction, the mixing factor  $X$  is estimated from the intensity ratio  $r_{23}$  of  $L_2$  to  $L_3$  as  $X = (2r_{23} - 1)/(r_{23} + 1)$  [18] and the spin correction factor (SC) is obtained as  $\text{SC} = 1/(1 - 2X)$ . For instance,  $\text{SC} = 3$  requires  $X = 1/3$  and  $r_{23} = 0.8$ . In the present XMCD experiments, we derive  $r_{23} = 0.62$ ,  $X = 0.15$ , and  $\text{SC} = 1.4$ . From these, we obtain 1.467 for the calibrated

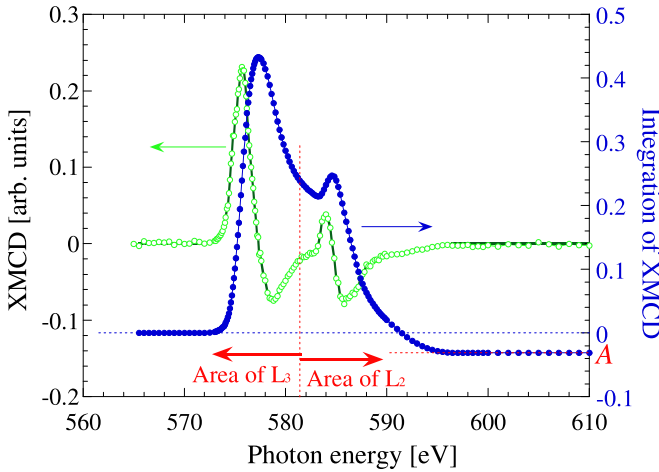


FIG. 5. XMCD spectrum  $\mu(+)-\mu(-)$  and its integral with respect to the energy. The border between the  $L_3$  and  $L_2$  regions, 581.3 eV, determined from the XAS minimum in Fig. 4(b), is shown.

$m_{\text{spin}}$  value ( $m'_{\text{spin}}$ ) as shown in Table III, a value approximately half of the  $3\mu_B$  observed in the bulk magnetization measurements [6,12]. The  $X$  depends on how an arctan step background is estimated, whereas it is now impossible to derive  $r_{23} = 0.8$ . Thus, in the present case, we conclude that the spin sum rule is useless.

## V. DFT RESULTS

In this section, ground-state DFT calculations are presented to support the previous discussion of the Cr local moments based on the XMCD measurement and, furthermore, to understand the role of the individual atomic SOC in the forced FM state.

In Sec. V A, in order to capture the fundamental aspects of the electronic structure of  $\text{CrNb}_3\text{S}_6$ , we first perform a spin-polarized scalar-relativistic calculation (without SOC) where the results do not depend on the magnetization direction. In particular, we focus on the hybridization of Cr  $3d$  orbitals. In Sec. V B, with SOC included, the easy-plane type MCA and Cr  $3d$  magnetic moments are discussed in detail. In Sec. V C, the individual roles of Cr and Nb SOC are analyzed.

### A. Electronic structure

Figure 6 shows the total density of states (DOS) calculated without SOC, which agrees well with those reported previously [12,27,28]. [We use the convention that spin up

TABLE III. Sum-rule based estimations of  $m_{\text{orb}}$  and  $m_{\text{spin}}$  in units of  $\mu_B$  based on nominal  $n_h = 7$  and theoretically predicted  $n_h = 5.84$ .

	$n_h = 7$	$n_h = 5.84$
$m_{\text{orb}}$	$-2.761 \times 10^{-2}$	$-2.303 \times 10^{-2}$
$m_{\text{spin}}$	1.048	$8.745 \times 10^{-1}$
$m'_{\text{spin}}$ (SC = 1.4)	1.467	1.224
$m_{\text{orb}}/3$	$-9.203 \times 10^{-3}$	$-7.677 \times 10^{-3}$

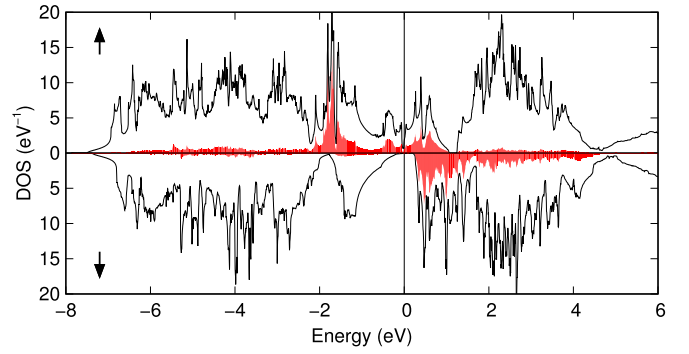


FIG. 6. Spin-up (upper panel) and spin-down (lower panel) density of states. Contributions from Cr valence  $l = 2$  states (within the muffin-tin sphere) are highlighted by red. Energy 0 refers to the Fermi level.

(down) denotes the majority (minority) spin.] S  $3p$  and Nb  $4d$  states are located mainly in the energy intervals  $[-8 : -2]$  and  $[-2 : 5]$  eV, respectively. Cr  $l = 2$  states (highlighted by red) show large exchange splitting: most of the spin-down states are pushed above  $E_F$ . Both spin channels are metallic with a finite DOS at  $E_F$ . Farther above  $E_F$ , a broad continuum feature starts from 5 eV in the DOS of both spins, indicating that the  $3d$  region ends at 5 eV. Indeed, above this energy, Cr  $l = 2$  partial waves become  $4d$ -like, picking up an additional radial node. We set  $E_c = 5$  eV in the analysis of the Cr  $3d$  shell using Eq. (12) discussed later.

Figure 7 shows partial  $d$ -wave DOS projected onto Nb hexagonal harmonics and Cr  $e'_g$ ,  $a_{1g}$ , and  $e_g$  harmonics (see Appendix B for the complete definition of these orbitals). The top two panels are for the Nb(2a) and (4f) sites while the bottom two are for Cr. We begin with the spin-up states shown in the left panels, Fig. 7(a). The  $e'_g$  states (the left lowest panel) form a sharp peak well below  $E_F$  in a narrow energy window (from  $-2$  to  $-1$  eV) that appears to be consistent with the localized  $t_{2g\uparrow}$  scheme. On the other hand, the rest of the  $t_{2g}$  manifold—the  $a_{1g}$  state (red highlighted in the second lowest panel)—is delocalized to a remarkable extent, spread over a wide energy range, even extending across  $E_F$  to the unoccupied levels, and with a similar bandwidth to the delocalized  $e_g$  state that hybridizes well with S  $3p$  orbitals. This unexpected  $a_{1g}$  delocalization is a consequence of strong hybridization with Nb  $4d$  orbitals. A clear indication of strong mixing is seen in the second panel: Nb(4f)  $z^2$  (red highlighted) has peak structures resonating with  $a_{1g}$ .

Regarding the spin-down bands, Fig. 7(b), the occupied states from  $-2$  eV and above are mainly Nb  $z^2$  and  $x^2 - y^2/xy$  orbitals. Although the exchange splitting pushes most of the spin-down Cr  $3d$  states above  $E_F$ , some of them come into the occupied levels and show a broader energy spectrum. They form chemical bonds with Nb and S orbitals and are (together with the spin-up  $3d$  states of the same character) magnetically dead. The states just at  $E_F$  are exclusively of Nb  $z^2$  character. The unoccupied body of spin-down states, starting from 0.2 eV, is composed of all  $d$  orbitals from Nb and Cr.

The method described in Eq. (12)—defining the Cr  $3d$  quantities as probed by the Cr  $2p$  core—is applied to the present non-SOC electronic structure. Table IV summarizes

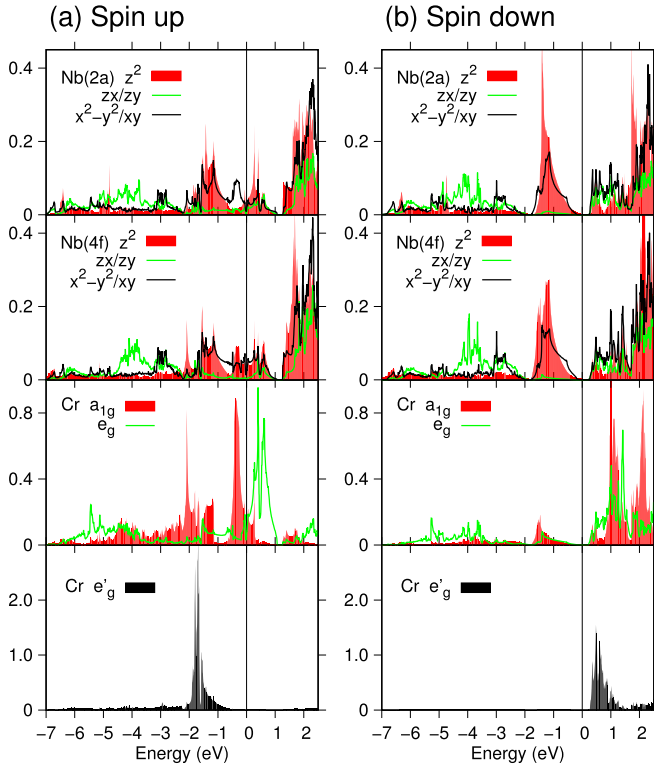


FIG. 7. Partial  $d$ -wave density of states (in unit of  $\text{eV}^{-1}$ ) projected onto Nb hexagonal harmonics and Cr  $e'_g$ ,  $a_{1g}$ , and  $e_g$  harmonics within the muffin-tin spheres for (a) spin up and (b) spin down. Multiplicity of atoms and orbitals is excluded. Note that the vertical scale is different in each panel.

the Cr  $3d$  occupation numbers obtained. The spin-up and -down  $3d$  states are about 3.6 and 0.6 electrons, respectively, yielding a total  $3d$  electron number of 4.16 ( $n_h = 5.84$ ) and a  $3d$  spin magnetic moment  $m_{\text{spin}} = 3.01\mu_B$ . Roughly speaking, there are 0.6 magnetically dead electrons in each spin; the magnetically active part exhibits an electron configuration  $(e'_g)^{1.8}(a_{1g})^{0.8}(e_g)^{0.5}$  for spin up, in sharp contrast to the localized picture with  $(t_{2g\uparrow})^3$ . The occupation number for  $a_{1g\uparrow}$  deviates from unity with some of  $e_{g\uparrow}$  states being occupied. Both  $a_{1g\uparrow}$  and  $e_{g\uparrow}$  states show up at  $E_F$  and contribute to the conductivity in the spin-up channel. Their metallic conduction may account for the relatively high  $T_c$  despite the rather long Cr-Cr interatomic distance.

### B. MCA and magnetic moment

Turning SOC on, we examine the MCA to see whether DFT reproduces the easy-plane-type anisotropy. The total-

TABLE IV. Cr  $3d$  occupation numbers calculated from the  $3d$  density matrix defined in Eq. (12).

Spin	$e'_g$	$a_{1g}$	$e_g$	Sum
up	1.88	0.89	0.82	3.59
down	0.08	0.13	0.36	0.58
up-down	1.80	0.76	0.45	3.01

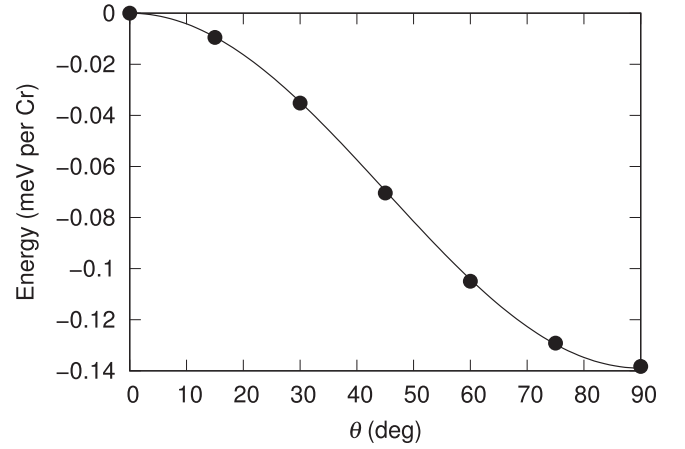


FIG. 8. Total-energy variation as a function of magnetization direction.  $\theta = 0$  ( $90$ ) degree corresponds to magnetization direction parallel (perpendicular) to the  $c$  axis. Dots represent the DFT energies while solid line shows a  $\sin^2\theta$  fit.

energy variation as a function of magnetization direction  $E(\theta, \phi)$  is calculated using the force theorem [29]. Figure 8 shows  $\Delta E(\theta) = E(\theta) - E(0)$  as a function of the polar angle  $\theta$  (the azimuth  $\phi$  dependency is negligibly small). The easy-plane-type anisotropy is correctly reproduced with an energy minimum located at  $\theta = 90^\circ$ . The energy variation follows a  $\sin^2\theta$  behavior (solid line), indicating that the MCA is dominated by the second-order effect of the SOC. The MCA energy, the energy difference between the hard-axis and easy-plane magnetizations, is found to be 0.14 meV per  $\text{CrNb}_3\text{S}_6$  unit, in a good agreement with the ESR experiment [14] and previous DFT calculations [28].

The spin magnetic moment with SOC turned on remains the same as that in the non-SOC case, and thus shows no dependence on the choice of magnetization direction. The total spin magnetic moment (obtained by integrating the spin density over the whole space) is  $3.004\mu_B$  per  $\text{CrNb}_3\text{S}_6$ , again consistent with the previous DFT result [28]. The contributions in each muffin-tin sphere are 2.500, 0.055, 0.003, and  $0.005\mu_B$ , from Cr, Nb(2a), Nb(4f), and S, respectively; a small positive spin moment is induced at the Nb(2a) site while the moments at the Nb(4f) and S sites are negligible. Figure 9 shows a two-dimensional spin-density map on a hexagonal ( $11\bar{2}0$ ) plane where Cr and Nb atoms are found. The spin density is peaked around Cr and extends with positive sign to a radius  $\sim 1.8 \text{ \AA}$ . The Nb(4f) site (sitting above and below Cr along  $c$ ) has sizable spin-density distribution with alternating signs even though it is integrated out to be nearly zero; in particular, a negative distribution along the  $c$  axis is clearly seen, which is a signature of the Cr  $a_{1g}$ -Nb  $z^2$  interaction.

Now we shift our focus to the Cr  $l = 2$  partial wave. Spin and orbital magnetization densities are shown in Fig. 10. The spin density is positive and has a large tail, well beyond the muffin-tin radius of  $1.1 \text{ \AA}$ ; the orbital density (displayed with multiplying a factor of 100) is predominately negative until turning positive at  $r \sim 1 \text{ \AA}$ . It is apparent that the spin and orbital moments are coupled antiparallel, as expected from an atomic picture for the less-than-half filled case. However, the quantitative values of the  $3d$  magnetic moments depend on the

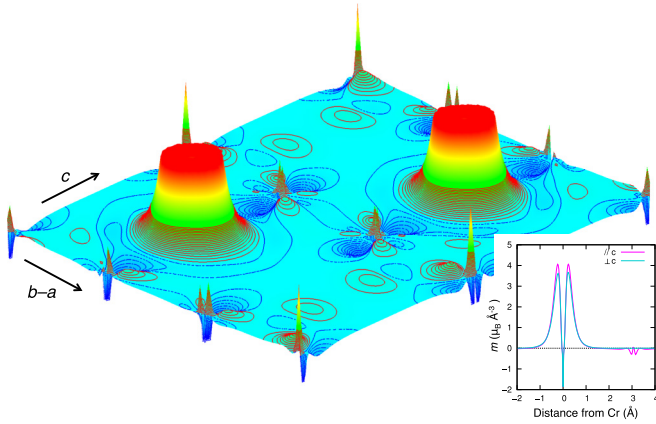


FIG. 9. Spin magnetization density mapped on a hexagonal ( $11\bar{2}0$ ) plane. The high density around the Cr is cut off, and the low-density region ( $<0.1\mu_B \text{ \AA}^{-3}$ ) is highlighted by contour lines; red (blue) lines are for small positive (negative) densities. Inset: one-dimensional plots of the spin magnetization density parallel and perpendicular to the  $c$  axis, on the ( $11\bar{2}0$ ) plane through Cr nucleus.

choice of integration region because of the tails in their density distributions. Furthermore, the  $l = 2$  partial wave (which is used in calculating the density distribution in Fig. 10) is not a pure Cr  $3d$  wave; at large  $r$  it includes orbital tails from the surrounding atoms. The Cr  $2p$  core function  $R_{2p}$  (shown by pale green in Fig. 10), however, is localized in a region close to the nucleus where the  $l = 2$  wave predominately originates from the Cr  $3d$  state. Using  $rR_{2p}$  as a probe for Cr  $3d$  state, we calculate local quantities in the  $3d$  shell as summarized

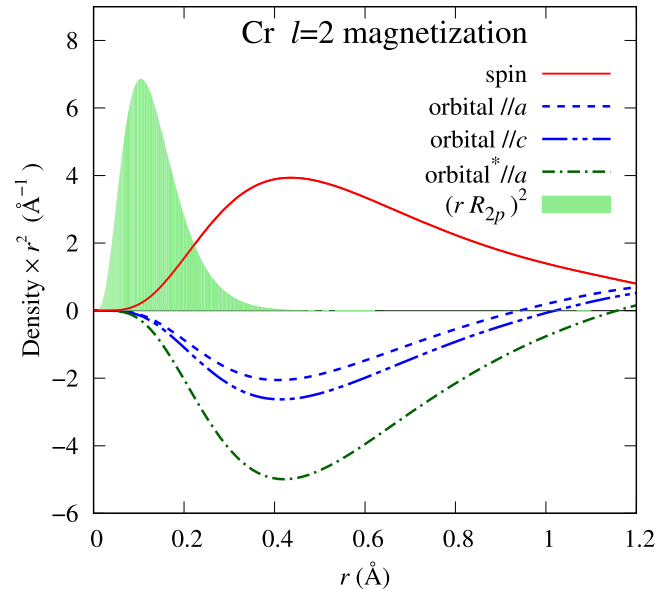


FIG. 10. Spin and orbital magnetization densities originating from the Cr  $l = 2$  partial wave. The spherical part of the density is multiplied by the weighting factor  $r^2$ . The orbital contributions are magnified by 100 relative to the spin, and are shown for magnetization along the  $a$  and  $c$  axes. The dash-dotted line (“orbital<sup>\*\*\*</sup>”) is obtained for the Cr-only SOC calculation (see Sec. VC for details). The radial density of the Cr  $2p$  core radial function  $R_{2p}$  is also shown.

TABLE V. Cr  $3d$  electron number, spin, and orbital magnetic moments ( $\mu_B$ ), and spin magnetic dipole calculated for two magnetization directions:  $a$  (easy axis) and  $c$  (hard axis). For the top two entries (“ $R_{2p}$ ”) the Cr  $2p$  core is used as a local probe, Eq. (12). The errors are estimated to be  $\pm 0.4\%$  for each quantity listed, determined by shifting the boundary energy  $E_c$  by  $\pm 0.5$  eV. The bottom two lines (“MT”) are calculated simply by integrating the  $l = 2$  partial wave within the Cr muffin-tin sphere.

Direction $\alpha$	$N$	$m_{\text{spin}}$	$m_{\text{orb}} \times 10^3$	$7\langle T_\alpha \rangle$
$R_{2p}$ : $a$	4.16	3.01	-16.3	-0.156
$c$	4.16	3.01	-20.1	0.308
MT: $a$	3.74	2.47	-9.4	-0.144
$c$	3.74	2.47	-13.3	0.286

in Table V. The Cr  $3d$  spin magnetic moment  $m_{\text{spin}}$  obtained is nearly  $3.0\mu_B$ , consistent with a proper picture that the Cr  $3d$  state is responsible for the magnetism in  $\text{CrNb}_3\text{S}_6$ , and is greatly enhanced from the  $l = 2$  muffin-tin value of  $2.5\mu_B$  (Table V). The Cr  $3d$  orbital moment  $m_{\text{orb}}$  is found to have a negative sign (antiparallel to the spin) with small values of  $-0.016\mu_B$  and  $-0.020\mu_B$  for the in-plane and out-of-plane magnetization, respectively. These values are enhanced from the  $l = 2$  muffin-tin values in Table V, indicating that the sign change of the orbital distribution at  $r \sim 1 \text{ \AA}$  (seen in Fig. 10) is not from the pure  $3d$  orbital but from hybridization effects that develop positive orbital distribution in the  $3d$  tail region. The ratio between orbital and spin is  $m_{\text{orb}}/m_{\text{spin}} \times 100 = -0.54$  (in-plane magnetization) and  $-0.69$  (out-of-plane). Naively it is counterintuitive that  $m_{\text{orb}}$  in the easy-plane magnetization has smaller magnitude than that in the hard-axis magnetization. We will come back to this point in the next subsection. The spin magnetic dipole shown in Table V obeys the relation  $\sum_{\alpha=x,y,z} \langle T_\alpha \rangle \sim 0$ , which is known to hold in the weak SOC case [30]. Ignoring its contribution in the application of the spin sum rule would degrade the estimated  $m_{\text{spin}}$  by only 5% for the in-plane magnetization. The Nb and S atoms have very small orbital moments (less than  $10^{-3}\mu_B$  for the in-plane magnetization), which we will not discuss further here.

The Cr  $3d$  electron number is calculated to be 4.16 (unchanged from the non-SOC calculation), which gives the number of holes in the  $3d$  shell,  $n_h = 5.84$ . Using this  $n_h$  in the XMCD orbital sum rule, the experimentally deduced  $m_{\text{orb}}$  is compared with the DFT value in Table VI. A fairly good agreement is achieved between the experiment and theory, especially taking into account the fact that the DFT tends to underestimate  $m_{\text{orb}}$ . We conclude that the order of  $m_{\text{orb}}/m_{\text{spin}}$  is  $\sim -1\%$ .

TABLE VI. Comparison between experimental and theoretical  $m_{\text{orb}}$  values for the in-plane magnetization. The DFT-estimated hole number,  $n_h = 5.84$ , is used in the XMCD orbital sum rule. The ratio  $m_{\text{orb}}/m_{\text{spin}}$  assumes  $m_{\text{spin}} = 3$ .

	$m_{\text{spin}}$	$m_{\text{orb}} \times 10^3$	$m_{\text{orb}}/m_{\text{spin}} (=3)$ (%)
theory	3.01	-16.3	-0.54
MCD		-23.0	-0.77

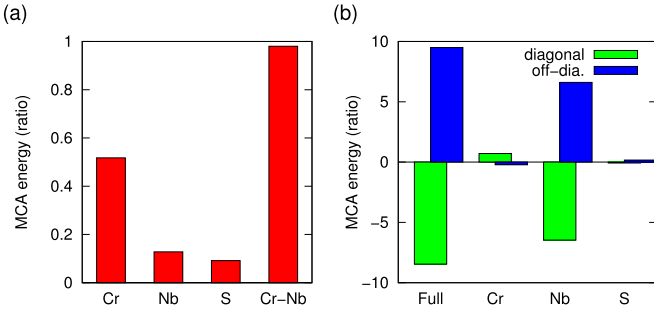


FIG. 11. (a) DFT-calculated MCA energies obtained by selectively turning on SOC for different elements, given as the ratio to the full MCA value (0.14 meV per CrNb<sub>3</sub>S<sub>6</sub>). (b) Same as (a) but decomposed into the spin-diagonal and spin-off-diagonal SOC processes. Note that the vertical scale is different from (a).

### C. Cr and Nb SOC

We have seen that the MCA is of easy-plane type and that the unquenched Cr 3*d* orbital moment is aligned antiparallel to the spin moment. There is no doubt that the SOC in the Cr 3*d* shell plays a major role. However, the spin-orbit coupling constant  $\lambda$  for the Nb 4*d* orbital (0.1 eV) is three times as large as that for Cr 3*d* orbital (0.034 eV) and thus Nb SOC may also play an important role.

In this section, we examine the individual atomic SOC and analyze in detail the origin of the easy-plane MCA. We turn on the SOC only at selected element(s) and calculate the MCA energy as summarized in Fig. 11(a). Turning on the Cr SOC alone provides 50% of the full MCA energy, indicating that the Cr SOC is indispensable (as expected) but the other elements provide some contributions. However, pure elemental SOC of Nb and S give very small MCA energies, 13% and 10%, respectively; the full MCA is not reproduced from the simple sum of these individual effects. When the Cr and Nb SOC are turned on together, 96% of the full MCA is reproduced. This clearly shows that the Nb SOC enhances the MCA, i.e., the Nb and Cr SOC interact constructively.

To further understand this enhancement of the MCA through the Nb SOC, we adopt a second-order perturbation theory. We write the unperturbed eigenstates (in the FM state without the SOC) as  $\{|\epsilon_i, \varphi_i\rangle\}$ , where  $i$  is a combined index of wave vector  $\mathbf{k}$ , spin  $\sigma$  ( $= \pm 1/2$ ), and band index  $n$ . The SOC perturbation depends on the magnetization direction  $\hat{\mathbf{m}}$  ( $|\hat{\mathbf{m}}| = 1$ ) and may be written as

$$H_{\hat{\mathbf{m}}}^{\text{SOC}} = H_{\text{SO}}(\hat{\mathbf{m}}) = U_{\hat{\mathbf{m}}}^{\dagger} H_{\text{SO}} U_{\hat{\mathbf{m}}} \quad (20)$$

with the spin rotation matrix  $U_{\hat{\mathbf{m}}}$  (see Appendix C) and with  $H_{\text{SO}}$  being a sum of atomic SOC Hamiltonian  $\lambda \mathbf{L} \cdot \mathbf{s}$  of Cr 3*d*, Nb 4*d*, and S 3*p* orbitals,

$$H_{\text{SO}} = H_{\text{SO}}^{(\text{Cr})} + H_{\text{SO}}^{(\text{Nb})} + H_{\text{SO}}^{(\text{S})}. \quad (21)$$

According to the force theorem [29], the MCA energy is given in terms of the band energy summation over occupied states,

$$E(\hat{\mathbf{m}}) = \sum_i f_i^{(\hat{\mathbf{m}})} \epsilon_i^{(\hat{\mathbf{m}})}, \quad E_{\text{MCA}} = E(\hat{\mathbf{m}} \parallel c) - E(\hat{\mathbf{m}} \perp c),$$

where  $f_i^{(\hat{\mathbf{m}})}$  and  $\epsilon_i^{(\hat{\mathbf{m}})}$  are the band occupation number and band energy with the perturbation incorporated. Using a

second-order perturbation theory and disregarding the change in the band occupation number (that is small in the present case), the band energy sum can be found as

$$E(\hat{\mathbf{m}}) = E_0 + \sum_{i,j} f_i(1-f_j) \frac{|\langle i|H_{\hat{\mathbf{m}}}^{\text{SOC}}|j\rangle|^2}{\epsilon_i - \epsilon_j} \delta_{\mathbf{k},\mathbf{k}'}, \quad (22)$$

where only a pair of occupied and unoccupied bands (at the same  $\mathbf{k}$ ) interacting via SOC contributes to the MCA through its  $\hat{\mathbf{m}}$  dependence. The relevant matrix element squared is decomposed as

$$|\langle i|H'|j\rangle|^2 = |\langle i|H_{\text{SO}}^{(\text{Cr})}|j\rangle|^2 + |\langle i|H_{\text{SO}}^{(\text{Nb})}|j\rangle|^2 + \langle i|H_{\text{SO}}^{(\text{Cr})}|j\rangle \langle j|H_{\text{SO}}^{(\text{Nb})}|i\rangle + \text{c.c.}, \quad (23)$$

where the  $\hat{\mathbf{m}}$  dependence and the sulfur related terms are suppressed for simplicity. In addition to the pure individual contributions [the first and second terms of Eq. (23)], a Cr-Nb *interference* term (the third term) exists as well, which may enhance the MCA effectively only if (i) strong hybridization between Cr 3*d* and Nb 4*d* orbitals is seen in both states  $i$  and  $j$  and (ii) the phases of two SO matrix elements constructively interfere. The DFT result given in Fig. 11(a) indicates that this Cr-Nb interference term doubles the MCA energy compared to that with the Cr SOC alone.

In Fig. 11(b), we further decompose the MCA into two spin processes: spin-diagonal (bands  $i$  and  $j$  have the same spin,  $\sigma_i = \sigma_j$ ) and spin-off-diagonal SOC process ( $\sigma_i \neq \sigma_j$ ). In the full SOC calculation [a set of two boxes located in the most left of Fig. 11(b)], two spin processes have fairly large energy (nearly one order of magnitude greater than the net MCA energy) while they compete with each other: the spin-off-diagonal process favors in-plane magnetization; the spin-diagonal process favors out-of-plane magnetization. In the case of the Cr-SOC only calculation, the spin-diagonal process (the interaction in the spin-up channel) dominates and provides the easy-plane anisotropy, where a pair of  $a_{1g\uparrow}$  and  $e_{g\uparrow}$  states should be most relevant. In the Nb-SOC only case, both spin processes have large values (similar to the full SOC calculation) but they almost cancel with different signs, resulting in the only 13% of the full MCA energy. That two processes have nearly identical magnitude is due to the fact that both spins are found in the occupied Nb 4*d* bands. The interference term, however, picks up bands that have substantial Cr 3*d*-Nb 4*d* mixing in their wave functions. Therefore, the occupied counterpart in the interference process is dominated by spin-up (due to the Cr 3*d* spin polarization). From the MCA decomposition analysis (Fig. 11) and the partial DOS analysis (Fig. 7), together with the matrix representation of  $\mathbf{L}$  (Appendix B), the occupied-unoccupied pairs of bands that are highly relevant to the MCA are identified as  $a_{1g\uparrow}$ - $e_{g\uparrow}$  (for the pure Cr SOC) and  $e_{g\uparrow}$ - $e'_{g\downarrow}$  (for the interference SOC).

The Cr 3*d* orbital moment behaves differently in the site-selective SOC calculations. First-order perturbation theory illustrates that the Cr orbital moment is given by

$$\langle L_{\alpha}^{(\text{Cr})} \rangle = \sum_{i,j} \frac{f_i(1-f_j)}{\epsilon_i - \epsilon_j} \times [\langle i|L_{\alpha}^{(\text{Cr})}|j\rangle \langle j|H'_{\alpha}|i\rangle \delta_{\sigma,\sigma'} \delta_{\mathbf{k},\mathbf{k}'} + \text{c.c.}], \quad (24)$$

TABLE VII. Cr  $3d$  orbital magnetic moment,  $m_{\text{orb}}$ , calculated by turning the SOC on only at selected element. In unit of  $10^{-3}\mu_B$ . Two magnetization directions, along  $a$  and  $c$  axes, are examined. The Cr  $2p$  local-probe technique is used.

Direction $\alpha$	Cr	Nb	S
$a$	-38.9	12.7	9.9
$c$	-32.0	7.8	3.5

where  $\alpha = x, y, z$ . Note that the right-hand size is linear in  $H'$  (sum of atomic SOC) and thus  $m_{\text{orb}}$  in the full SOC calculation is determined by a simple summation of elemental SOC effects. Table VII lists the values of  $3d$  orbital moment in the element-selective SOC calculations. The summation of these values indeed reproduce  $m_{\text{orb}}$  in the full SOC calculation (Table V). It is interesting to see that in the Cr-only SOC calculation  $m_{\text{orb}}$  is much larger than its full SOC value and now the in-plane  $|m_{\text{orb}}|$  is greater than that for the out-of-plane (hard-axis) magnetization. The Nb- and S-only SOC calculations yield opposite-sign orbital moments in the Cr  $3d$  shell. From these results we conclude that SOC on the Nb and S atoms interfere destructively to decrease the Cr orbital moment.

## VI. CONCLUSION

We have performed the XAS/XMCD measurements for  $\text{CrNb}_3\text{S}_6$  with in-plane magnetization at the Cr  $L_{2,3}$  edges. The XMCD spectrum, exhibiting dispersive line shapes for each of the  $L_3$  and  $L_2$  edges, unambiguously reveals that the Cr orbital magnetic moment is not quenched and is coupled antiparallel to the spin counterpart. The magnitude of orbital magnetic moment is estimated to be approximately  $0.02\mu_B$ . The quantitative evaluation of spin magnetic moment via the sum rules is unsuccessful due to the small spin-orbit splitting in the Cr  $2p$  core. These experimental findings on the Cr local magnetism are supported by the DFT calculations, where, analogous to the experiment, the radial part of the Cr  $2p$  core state is employed to define the  $3d$  shell. Theoretical analyses show that the SOC in the Nb  $4d$  orbital, as a consequence of its strong hybridization with the Cr  $3d$  orbital, plays an important role in determining the MCA and the Cr  $3d$  orbital moment.

## ACKNOWLEDGMENTS

This work was supported by Grants-in-Aid for Scientific Research, Grant No. (S) 25220803, from the Ministry of Education, Culture, Sports, Science and Technology (MEXT), Japan; the Center for Chiral Science in Hiroshima University (the MEXT program for promoting the enhancement of research universities, Japan); JSPS Core-to-Core Program, A. Advanced Research Networks; and the National Science Foundation, Grant No. EFMA-1741673. The synchrotron radiation experiments were performed at the BL25SU in SPring-8 with the approval of the Japan Synchrotron Radiation Research Institute (JASRI) (Proposals No. 2015B1018 and No. 2016A1029).

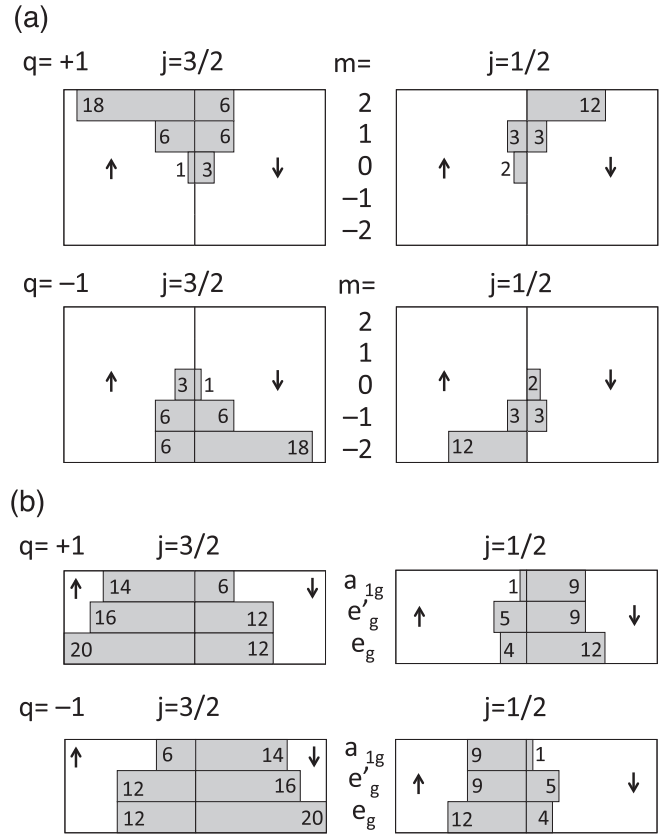


FIG. 12. Distribution of weights of the transition probability to the  $d$  states in the  $p \rightarrow d$  photoabsorption process with the photon spin  $q = \pm 1$  when the core hole  $j$  is a good quantum number. (a)  $d$  states labeled by the orbital magnetic quantum number  $m$  (after Ref. [26]). (b)  $d$  states under the  $D_{3d}$  crystalline field. The magnetization and the photopropagation directions are perpendicular to the threefold ( $z$ ) axis.

## APPENDIX A: TRANSITION PROBABILITY

Imada *et al.* have tabulated the transition probability in the  $p \rightarrow d$  photoabsorption when the core hole  $j$  is a good quantum number and the  $d$  states are labeled by the spin and the orbital magnetic quantum number [26]. Figure 12(a) reproduces their result; Fig. 12(b) is for the case that the  $d$  states are labeled by  $a_{1g}$ ,  $e'_g$ , and  $e_g$  manifolds (under the  $D_{3d}$  crystalline field) with both the magnetic field and the photopropagation being perpendicular to the threefold axis.

## APPENDIX B: $d$ ORBITAL

The hexagonal harmonics ( $z^2, zx, zy, x^2 - y^2, xy$ ) defined in the coordinate system  $(x, y, z)$  in Fig. 1(b) are considered the natural basis functions for Nb  $4d$  states. In this basis set, the orbital angular momentum operator is given in the matrix representation

$$L_x = \begin{pmatrix} 0 & 0 & \sqrt{3}i & 0 & 0 \\ 0 & 0 & 0 & 0 & i \\ -\sqrt{3}i & 0 & 0 & -i & 0 \\ 0 & 0 & i & 0 & 0 \\ 0 & -i & 0 & 0 & 0 \end{pmatrix},$$

$$L_y = \begin{pmatrix} 0 & -\sqrt{3}i & 0 & 0 & 0 \\ \sqrt{3}i & 0 & 0 & -i & 0 \\ 0 & 0 & 0 & 0 & -i \\ 0 & i & 0 & 0 & 0 \\ 0 & 0 & i & 0 & 0 \end{pmatrix},$$

$$L_z = \begin{pmatrix} 0 & 0 & 0 & 0 & 0 \\ 0 & 0 & -i & 0 & 0 \\ 0 & i & 0 & 0 & 0 \\ 0 & 0 & 0 & 0 & -2i \\ 0 & 0 & 0 & 2i & 0 \end{pmatrix}.$$

In the main text, Cr 3d states are discussed in terms of  $a_{1g}$ ,  $e'_g$ , and  $e_g$  manifold (which is valid under  $D_{3d}$  symmetry). The trigonal basis functions,  $x_0$  (for  $a_{1g}$ ),  $x_{\pm}$  (for  $e'_g$ ),  $u_{\pm}$  (for  $e_g$ ), are given as follows:

$$\begin{aligned} x_0 &= Y_{20}, \\ x_+ &= -\sqrt{\frac{2}{3}}Y_{2-2} - \sqrt{\frac{1}{3}}Y_{21}, \\ x_- &= \sqrt{\frac{2}{3}}Y_{22} - \sqrt{\frac{1}{3}}Y_{2-1}, \\ u_+ &= -\sqrt{\frac{1}{3}}Y_{2-2} + \sqrt{\frac{2}{3}}Y_{21}, \\ u_- &= \sqrt{\frac{1}{3}}Y_{22} + \sqrt{\frac{2}{3}}Y_{2-1}, \end{aligned}$$

where the spherical harmonics are defined in the coordinate system  $(x, y, z)$  in Fig. 1(b). The orbital angular momentum operator is written in the matrix form with the basis  $(x_0, x_+, x_-, u_+, u_-)$ ,

$$L_x = \begin{pmatrix} 0 & -1/\sqrt{2} & -1/\sqrt{2} & 1 & 1 \\ -1/\sqrt{2} & 0 & 0 & 0 & -1 \\ -1/\sqrt{2} & 0 & 0 & 1 & 0 \\ 1 & 0 & 1 & 0 & 0 \\ 1 & -1 & 0 & 0 & 0 \end{pmatrix},$$

$$L_y = \begin{pmatrix} 0 & -i/\sqrt{2} & i/\sqrt{2} & i & -i \\ i/\sqrt{2} & 0 & 0 & 0 & -i \\ -i/\sqrt{2} & 0 & 0 & -i & 0 \\ -i & 0 & i & 0 & 0 \\ i & i & 0 & 0 & 0 \end{pmatrix},$$

$$L_z = \begin{pmatrix} 0 & 0 & 0 & 0 & 0 \\ 0 & -1 & 0 & -\sqrt{2} & 0 \\ 0 & 0 & 1 & 0 & \sqrt{2} \\ 0 & -\sqrt{2} & 0 & 0 & 0 \\ 0 & 0 & \sqrt{2} & 0 & 0 \end{pmatrix}.$$

### APPENDIX C: SOC HAMILTONIAN

We write the atomic SOC Hamiltonian as

$$H_{\text{SO}} = \lambda \mathbf{L} \cdot \mathbf{s} = \frac{\lambda}{2} \begin{pmatrix} L_z & L_x - iL_y \\ L_x + iL_y & -L_z \end{pmatrix}$$

for the spin basis functions (up and down) defined along the crystalline  $z$  axis. The SOC Hamiltonian with the spin quantization axis along an arbitrary direction  $\hat{\mathbf{m}}$  (with polar angle  $\theta$  and azimuthal angle  $\phi$ ) is found in the following, by using the spin rotation matrix  $U_{\hat{\mathbf{m}}}$  [31],

$$H_{\text{SO}}(\hat{\mathbf{m}}) = U_{\hat{\mathbf{m}}}^\dagger H_{\text{SO}} U_{\hat{\mathbf{m}}} = \frac{\lambda}{2} \begin{pmatrix} \mathbf{L} \cdot \hat{\mathbf{m}} & \mathbf{L} \cdot \tilde{\mathbf{e}} \\ \mathbf{L} \cdot \tilde{\mathbf{e}}^* & -\mathbf{L} \cdot \hat{\mathbf{m}} \end{pmatrix},$$

and

$$\hat{\mathbf{m}} = (\sin \theta \cos \phi, \sin \theta \sin \phi, \cos \theta)^T,$$

$$\tilde{\mathbf{e}} = (\cos \theta \cos \phi + i \sin \phi, \cos \theta \sin \phi - i \cos \phi, -\sin \theta)^T,$$

where  $\hat{\mathbf{m}}$  is the directional cosine of the spin quantization axis, and  $\tilde{\mathbf{e}}$  is a complex vector ( $|\tilde{\mathbf{e}}|^2 = 2$ ) orthogonal to  $\hat{\mathbf{m}}$ . For [001], [100], and [010] directions, the SOC Hamiltonians are

$$H_{\text{SO}}[001] = \frac{\lambda}{2} \begin{pmatrix} L_z & L_x - iL_y \\ L_x + iL_y & -L_z \end{pmatrix},$$

$$H_{\text{SO}}[100] = \frac{\lambda}{2} \begin{pmatrix} L_x & -iL_y - L_z \\ iL_y - L_z & -L_x \end{pmatrix},$$

$$H_{\text{SO}}[010] = \frac{\lambda}{2} \begin{pmatrix} L_y & iL_x - L_z \\ -iL_x - L_z & -L_y \end{pmatrix}.$$

[1] I. E. Dzyaloshinskii, *J. Phys. Chem. Solids* **4**, 241 (1958).

[2] T. Moriya, *Phys. Rev.* **120**, 91 (1960).

[3] I. E. Dzyaloshinskii, *Zh. Eksp. Teor. Fiz.* **47**, 992 (1964) [*Sov. Phys. JETP* **20**, 665 (1965)].

[4] J. Kishine, K. Inoue, and Y. Yoshida, *Suppl. Prog. Theor. Phys.* **159**, 82 (2005).

[5] Y. Togawa, Y. Kousaka, K. Inoue, and J. Kishine, *J. Phys. Soc. Jpn.* **85**, 112001 (2016).

[6] T. Miyadai, K. Kikuchi, H. Kondo, S. Sakka, M. Arai, and Y. Ishikawa, *J. Phys. Soc. Jpn.* **52**, 1394 (1983).

[7] Y. Togawa, Y. Kousaka, S. Nishihara, K. Inoue, J. Akimitsu, A. S. Ovchinnikov, and J. Kishine, *Phys. Rev. Lett.* **111**, 197204 (2013).

[8] Y. Togawa, T. Koyama, Y. Nishimori, Y. Matsumoto, S. McVitie, D. McGrouther, R. L. Stamps, Y. Kousaka, J. Akimitsu, S. Nishihara, K. Inoue, I. G. Bostrem, V. E. Sinityn, A. S. Ovchinnikov, and J. Kishine, *Phys. Rev. B* **92**, 220412(R) (2015).

[9] H. Flack, *Helv. Chim. Acta* **86**, 905 (2003).

[10] M. Nespolo, *Cryst. Res. Technol.* **50**, 413 (2015).

- [11] M. Mito, T. Tajiri, K. Tsuruta, H. Deguchi, J. Kishine, K. Inoue, Y. Kousaka, Y. Nakao, and J. Akimitsu, *J. Appl. Phys.* **117**, 183904 (2015).
- [12] N. J. Ghimire, M. A. McGuire, D. S. Parker, B. Sipos, S. Tang, J.-Q. Yan, B. C. Sales, and D. Mandrus, *Phys. Rev. B* **87**, 104403 (2013).
- [13] K. Tsuruta, M. Mito, H. Deguchi, J. Kishine, Y. Kousaka, J. Akimitsu, and K. Inoue, *Phys. Rev. B* **93**, 104402 (2016).
- [14] D. Yoshizawa, J. Kishine, Y. Kousaka, Y. Togawa, M. Mito, J. Akimitsu, K. Inoue, and M. Hagiwara, *Phys. Proc.* **75**, 926 (2015).
- [15] M. Shinozaki, S. Hoshino, Y. Masaki, J. Kishine, and Y. Kato, *J. Phys. Soc. Jpn.* **85**, 074710 (2016).
- [16] P. Carra, B. T. Thole, M. Altarelli, and X. Wang, *Phys. Rev. Lett.* **70**, 694 (1993).
- [17] Y. Teramura, A. Tanaka, and T. Jo, *J. Phys. Soc. Jpn.* **65**, 1053 (1996).
- [18] E. Goering, *Philos. Mag.* **85**, 2895 (2005).
- [19] P. K. Majumdar, R. K. Mukherjee, and A. K. Banerjee, *Phys. Rev. B* **41**, 65 (1990).
- [20] B. T. Thole, P. Carra, F. Sette, and G. van der Laan, *Phys. Rev. Lett.* **68**, 1943 (1992).
- [21] N. Marzari and D. Vanderbilt, *Phys. Rev. B* **56**, 12847 (1997).
- [22] M. Mito, H. Ohsumi, K. Tsuruta, Y. Kotani, T. Nakamura, Y. Togawa, M. Shinozaki, Y. Kato, J.-i. Kishine, J.-i. Ohe, Y. Kousaka, J. Akimitsu, and K. Inoue, *Phys. Rev. B* **97**, 024408 (2018).
- [23] T. Nakamura, T. Muro, F. Guo, T. Matsushita, T. Wakita, T. Hirono, Y. Takeuchi, and K. Kobayashi, *J. Electron Spectrosc. Relat. Phenom.* **144-147**, 1035 (2005).
- [24] M. Weinert, G. Schneider, R. Podloucky, and J. Redinger, *J. Phys.: Condens. Matter* **21**, 084201 (2009).
- [25] J. P. Perdew, K. Burke, and M. Ernzerhof, *Phys. Rev. Lett.* **77**, 3865 (1996).
- [26] S. Imada, S. Suga, and T. Miyahara, *BUTSURI* **55**, 20 (2000) (in Japanese; Physical Society of Japan).
- [27] A. C. Bornstein, B. J. Chapman, N. J. Ghimire, D. G. Mandrus, D. S. Parker, and M. Lee, *Phys. Rev. B* **91**, 184401 (2015).
- [28] S. Mankovsky, S. Polesya, H. Ebert, and W. Bensch, *Phys. Rev. B* **94**, 184430 (2016).
- [29] M. Weinert, R. E. Watson, and J. W. Davenport, *Phys. Rev. B* **32**, 2115 (1985).
- [30] T. Oguchi and T. Shishidou, *Phys. Rev. B* **70**, 024412 (2004).
- [31] Y. Uratani, T. Shishidou, and T. Oguchi, *J. Phys. Soc. Jpn.* **78**, 084709 (2009).